PCCP

PAPER

View Article Online
View Journal | View Issue



Cite this: *Phys. Chem. Chem. Phys.*, 2015, **17**, 25114

# Assembly and relaxation behaviours of phosphatidylethanolamine monolayers investigated by polarization and frequency resolved SFG-VS†

Feng Wei,*[a] Wei Xiong,[a] Wenhui Li,[a] Wangting Lu,[a] Heather C. Allen[b] and Wanquan Zheng[ac]

Received 9th July 2015,
Accepted 13th August 2015

DOI: 10.1039/c5cp03977k

www.rsc.org/pccp

The assembly conformation and kinetics of phosphatidylethanolamine (PE) lipids are the key to their membrane curvatures and activities, such as exocytosis, endocytosis and Golgi membrane fusion. In the current study, a polarization and frequency resolved (bandwidth $\approx$ 1 $cm^{-1}$) picosecond sum frequency generation (SFG) system was developed to characterize phosphatidylethanolamine monolayers. In addition to obtaining $\pi$–A isotherms and Brewster angle microscopy (BAM) images, the conformational changes and assembly behaviors of phosphatidylethanolamine molecules are investigated by analyzing the SFG spectra collected at various surface pressures (SPs). The compression kinetics and relaxation kinetics of phosphatidylethanolamine monolayers are also reported. The conformational changes of PE molecules during the monolayer compression are separated into several stages: reorientation of the head group $PO_2^-$ in the beginning of the liquid-expanded (LE) phase, conformational changes of head group alkyl chains in the LE phase, and conformational changes of tail group alkyl chains in the LE–liquid condensed (LE–LC) phase. Such an understanding may help researchers to effectively control the lipid molecular conformation and membrane curvatures during the exocytosis/endocytosis processes.

## 1 Introduction

Phosphatidylethanolamine (PE) is a critically important zwitterionic phospholipid within the cell membrane, and is the second most abundant phospholipid in mammalian cells, with an abundance of approximately 25%. The proportion of PE in the brain can be as high as 45%.[1] The inner membranes of mitochondria are also enriched in PE lipids compared to other membranes.[1] The decrease in the proportion of PE in the mitochondrial membranes of yeast, *T. brucei* and in mammalian cells can greatly change the membrane morphologies.[2,3] PE molecules are also frequently involved in many membrane activities, such as exocytosis, endocytosis and Golgi membrane fusion.[4–6] It has been reported that PE facilitates the exocytosis process and accelerates the expulsion of a neurotransmitter in PC12 cells.[4] It has also been proposed that a lack of PE lipid may impair membrane fusion and cause inhibition of the cell cycle in the parasite *T. brucei*.[3] Prevalent usages of PE in drug delivery and gene therapy as components of lipid raft or aerosol have been reported in the literature.[7,8] With the mediation of peptides, cholesterols, pH values and divalent ions, PE can facilitate the delivery of DNA and RNA molecules to target cells by membrane fusion and cell penetration.[9,10] Yet, the specific role of PE, or the exact mechanism of action, in these membrane activities is not fully understood yet.[11–15]

The assembly and relaxation behaviors of PE lipids are the key to their membrane activities.[12–14] The phase transition and assembly behaviors of lipid molecules in model systems of lipid monolayers, have been studied using characterization techniques, such as infrared reflection absorption spectroscopy (IRRAS),[16] Brewster angle microscopy (BAM),[9,16] and grazing incidence X-ray diffraction (GIXD).[12,14] Sum frequency generation vibrational spectroscopy (SFG-VS) is nonlinear vibrational spectroscopy with the merits of interface specificity and monolayer sensitivity,[17–19] which enable the characterization of structural and conformational changes of lipid molecules in the interfacial environment. Cholesterol induced condensation of DPPC (dipalmitoylphosphatidylcholine) monolayers has been elucidated by Bonn *et al. via* femto-second broad-band SFG-VS (BB-SFG-VS)

[a] *Institution for Interdisciplinary Research, Jianghan University, Building J13, Room C202, 8th Triangle Lake Road, Zhuankou District, Wuhan, Hubei, 430056, China. E-mail: weifeng@jhun.edu.cn*
[b] *Department of Chemistry and Biochemistry, The Ohio State University, 100 West 18th Avenue, Columbus, OH 43210, USA*
[c] *Institut des Sciences Moléculaires d'Orsay, Université de Paris-Sud, 91405, ORSAY Cedex, France*

† Electronic supplementary information (ESI) available: Details about $\pi$–A isotherm and BAM experiments, SFG data analysis. See DOI: 10.1039/c5cp03977k

 

based on the alkyl chain spectra (2700–3100 $cm^{-1}$).[20,21] The conformation, surface orientation and hydration of deuterated DPPC tail and head groups have been characterized by Ma *et al. via* BB-SFG-VS.[22–24] SFG-VS is also capable of capturing the changes of ordering, hydration and orientations of lipid molecules during their its interaction with ions, such as, Na+, $Ca^{2+}$ and thiocyanate ($SCN^-$).[25–27] The duramycin-lipid[28] and DNA–lipid interactions[29] were also investigated *via* SFG-VS at the lipid monolayer/water interface. The influence of poly(ethylene oxide) chains on the phase transitions behaviors of L-*R*-distearoyl phosphatidylethanolamine (DSPE) was investigated by C. Ohe *et al.* by BB-SFG-VS.[30] The interfacial conformations of phosphatidylethanolamine lipids are also investigated extensively by P. J. Kett *et al.*[31–34] To understand the water molecular structures and orientations at the lipid monolayer/water interface, new techniques, such as phase-sensitive BB-SFG-VS[35–37] and heterodyne-detected SFG-VS,[38] were also developed. In addition, polarization-resolved SFG-VS was also developed by Smits *et al.* to detect DPPC monolayer relaxation behaviors.[39,40]

Most of above investigations were accomplished by BB-SFG-VS, with the spectra resolution more than 10 $cm^{-1}$, which is less than optimal value to capture the structural details of lipids in the interface region. In the current study, a polarization and frequency resolved picosecond SFG system was developed to characterize the assembly and relaxation behaviors of PE lipid monolayers. The robustness of frequency-resolved SFG-VS for characterizing the structure and conformational details has already been shown by the investigations of 4-*n*-octyl-4-cyanobiphenyl (8CB), limonene and DMSO molecules at the interface.[41–44] The spectral resolution of the current SFG system is $\approx$1 $cm^{-1}$. Using such a system, the assembly conformations and relaxation kinetics of PE molecules are characterized accurately and efficiently.

## 2 Experimental

The pico-second SFG system was purchased from EKSPLA, Lithuania. Two laser beams at 1064 nm with a pulse duration of 30 ps are generated from the PL2251 mode-locked Nd:YAG laser. One of the 1064 nm beams (amplified in PL2251, $\approx$33 mJ, 20 Hz) is used to generate the first 532 nm beam for SFG-VS experiments, and the second 532 nm beam for optical parametric amplification (OPA), and the 1064 nm beam for differential frequency generation (DFG). The other 1064 nm beam (Train, 87.2 MHz) is utilized to generate 532 nm train beam for the synchronously pumped optical parametric oscillator (OPO) system after amplification. The seed beam within the wavelength range of 680–1064 nm with a bandwidth of $<$0.2 nm ($<$1.6 $cm^{-1}$) can be generated by the OPO system.[45] After the seed laser beam overlaps with the second 532 nm beam in the OPA system and the 1064 nm beam DFG system, the IR beam within the wavenumber range of 650–4000 $cm^{-1}$ can be generated. The bandwidth of the final IR beam is calculated to be $\approx$1 $cm^{-1}$, about twice the transform-limited width of a 30 ps Gaussian pulse (0.48 $cm^{-1}$). With such a bandwidth, the SFG spectra distortion can be less than 1% in most molecular groups (shown in Table 1). At this level of spectral distortion, the intrinsic molecular lineshapes obtained by the current SFG system will provide a better understanding of the structural and conformational changes during the interfacial assembly of PE lipids.

Table 1 SFG spectra distortions at different bandwidths

| $\Delta\nu_H$[a] | $\Delta\nu_I$ | $\Delta\nu_{Instr}$ | $\Delta\nu_{Voigt}$ Origin | $\Delta\nu_{Voigt}$ Total | Distortion (%) |
|---|---|---|---|---|---|
| 4.7 | 8.1 | 5[b] | 10.9 | 12.3 | 12.6 |
| | | 2[c] | | 11.1 | 2.2 |
| | | 1 | | 11.0 | 0.5 |
| | | 0.55[d] | | 10.9 | 0.2 |
| 3.1 | 6.5 | 5 | 8.3 | 10.0 | 20.1 |
| | | 2 | | 8.6 | 3.5 |
| | | 1 | | 8.4 | 0.9 |
| | | 0.55 | | 8.3 | 0.3 |

[a] All units in $cm^{-1}$. [b] $\Delta\nu_{Instr}$ in most EKSPLA picosecond SFG systems, 2 $cm^{-1}$ resolution can achieved in the wavenumber range of 3000–4000 $cm^{-1}$. [c] $\Delta\nu_{Instr}$ in most EKSPLA picosecond SFG systems, 2 $cm^{-1}$ resolution can achieved in the wavenumber range of 3000–4000 $cm^{-1}$. [d] $\Delta\nu_{Instr}$ reported in ref. 42.

Polarization-resolved BB-SFG-VS detection has been shown previously by setting the polarization of the visible beam at 45° (or −45°) enabling separation of the signals at different polarizations with a polarization displacement prism.[39] Our approach in the pico-second SFG system differs slightly (check Scheme 1 for details). The ssp (the first "s" indicates that the detection polarization for SFG signal is S, the second "s" indicates that the incident visible beam is S-polarized, "p" indicates that the incident IR beam is P-polarized) signal and the ppp signal are separated by a polarization splitter, and the separated signals are detected by two sets of identical detection systems (Monochromator 3501/3504, SOLAR TII and PMT R7899, Hamamatsu) after the beam has gone through Glan polarizers, half-wave plates, filters and focusing lens separately. The polarization of the visible beam was changed by a motorized rotation stage.

The ssp and ppp spectra of PE monolayers were collected within the wavenumber range of 2800–3000 $cm^{-1}$ and 1000–1200 $cm^{-1}$ at a spectral resolution of 2 $cm^{-1}$. The visible beam

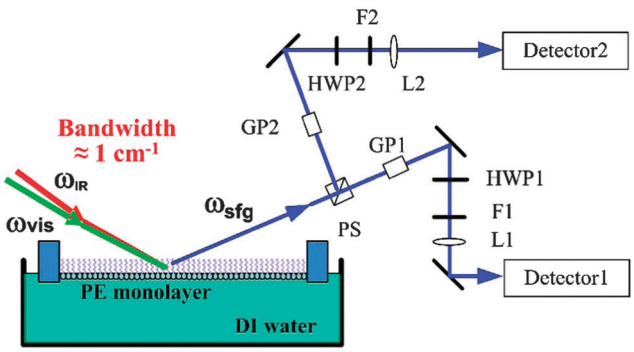


Scheme 1 Experimental setup of the polarization-resolved SFG-VS detection. PS: polarization splitter, GP: Glan-laser polarizer, HWP: half-wave plate, F: filter, L: lens.

and IR beam are focused onto the air/water interface at incident angles of 63° and 52° respectively. The SFG signals of each wavenumber were averaged at least 150 times. The intensities of ssp and ppp spectra are calibrated by normalizing to a *z*-cut quartz at a rotational angle of 0° (which has a SFG response only in the ssp and ppp polarization combinations). All the experiments are carried out in a controlled room environment (room temperature 22 ± 1 °C and humidity less than 40%). Additional details of π–A isotherm and BAM experiments are provided in the ESI.†

# 3 Results and discussion

## 3.1 Isotherm and BAM images

The π–A isotherm curves and BAM images of DMPE and DPPE (Scheme 2) monolayers are shown in Fig. 1 (see the ESI† for the experimental details of the π–A isotherm and BAM images). As seen in Fig. 1, the SP of DMPE monolayer increases at a mean molecular area (MMA) of 76 Å$^2$, and reaches a plateau (SP = 6.5–10 mN m$^{-1}$) at a molecular area of 56 Å$^2$ after going through the liquid-expanded (LE) phase. This plateau is also called the LE–LC phase transition region. It should be noted that the rising point of SP in our experiments is smaller than that reported in previous literature (~82 Å$^2$); however, our experiments were conducted at 22 °C (smaller than the temperature of 25 °C reported in the literature).[46] After the gradual increase during the compression prior to and within the plateau area, the SP of the DMPE monolayer increases significantly at a MMA of 35 Å$^2$ in the liquid-condensed (LC) phase. The SP of the DMPE monolayer then reaches a second plateau, which is called the collapse phase, at a MMA of 28 Å$^2$. On the other hand, DPPE monolayer shows much less compression elasticity. The SP of the DPPE monolayer increases at a MMA of 58 Å$^2$, and continues straight through the LE and LC phase to the collapse phase at a MMA of 42 Å$^2$.

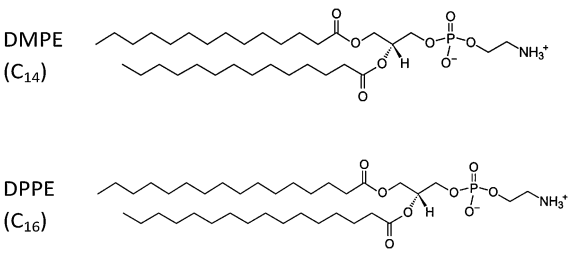


Scheme 2 Molecular structures of PE molecules.

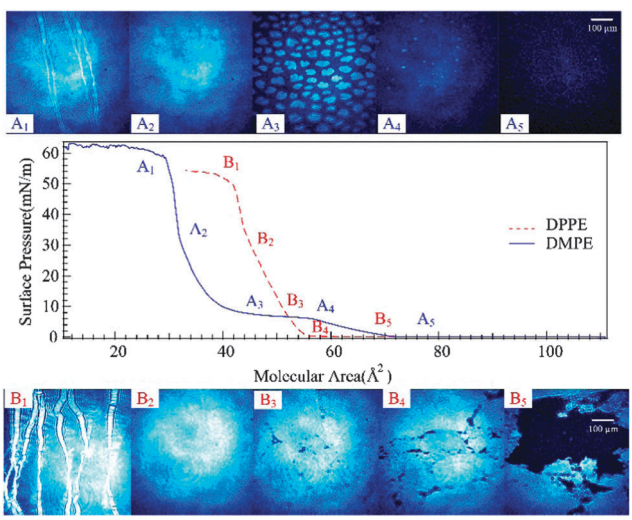


Fig. 1 π–A isotherm curves and BAM images of DMPE (blue solid line) and DPPE (red dashed line) monolayer at the collapse phase ($A_1$, $B_1$), LC phase ($A_2$, $B_2$), LE–LC phase ($A_3$, $B_3$), LE phase ($A_4$, $B_4$) and Gas–LE phase ($A_5$, $B_5$).

Table 2 The molecular area and surface pressures where the BAM images were taken

| | DMPE monolayer | | | DPPE monolayer | |
|---|---|---|---|---|---|
| | MMA (Å$^2$) | SP (mN m$^{-1}$) | | MMA (Å$^2$) | SP (mN m$^{-1}$) |
| $A_5$ | 80 | 0.033 | $B_5$ | 82.0 | 0.022 |
| $A_4$ | 58.6 | 5.0 | $B_4$ | 61.0 | 0.19 |
| $A_3$ | 52.7 | 6.6 | $B_3$ | 52.0 | 7.1 |
| $A_2$ | 33.2 | 26.2 | $B_2$ | 45.0 | 30.4 |
| $A_1$ | 20.7 | 62.5 | $B_1$ | 36.1 | 53.8 |

The BAM images of the DMPE and DPPE monolayers at the point of collapse ($A_1$, $B_1$), in LC ($A_2$, $B_2$), LE–LC ($A_3$, $B_3$), LE ($A_4$, $B_4$) and Gas–LE ($A_5$, $B_5$) phases (Table 2) are also shown in Fig. 1. As seen in Fig. 1, the BAM images of DMPE and DPPE monolayers at the collapse phase and LC phase are almost identical, and those in the LE–LC, LE and Gas–LE phases are different. Liquid-like domains with round edges are shown in the BAM image ($A_5$) of the Gas–LE phase of the DMPE monolayer. As for the DPPE monolayer, the solid-like domains with sharp edges are mostly observed in the Gas–LE phase. It is clear that the brightness of domains in the DPPE BAM image are much higher than that of the DMPE BAM image, revealing the lower thickness of the DMPE domains. The DMPE monolayer shows multiple lobular-like domains in the LE–LC phase, which is consistent with the BAM results in previous reports. The brightness of such lobular-like domains of DMPE are similar to that of the DPPE monolayer in the Gas–LE phase, indicating that their thicknesses are similar.[47] By comparing the brightness of different BAM images in different phases, it can be concluded that the thickness of the DMPE monolayer increases in the LE–LC phase by the formation of a multiple domain during the compression, but the thickness of the DPPE monolayer does not change too much (which is consistent with its lower compression elasticity).

## 3.2 Conformational changes of PE alkyl chains

Both ssp spectra and ppp spectra of the lipid monolayers were collected simultaneously by setting the polarization angle of the visible beam to 45°. The influence of environmental changes, such as sample dehydration and water height level, on the intensities of ssp and ppp spectra can be ruled out by such geometry. However, it should be noted that the SFG intensities collected from two detectors under such geometry are actually $I_1(\Omega = 45^\circ) = C_1|\chi^{(2)}_{ssp} + \chi^{(2)}_{spp}|^2$ and $I_2(\Omega = 45^\circ) = C_2|\chi^{(2)}_{psp} + \chi^{(2)}_{ppp}|^2$.[48]

 

Due to the isotropic structure of the lipid monolayer at the air/water interface, the contribution of $\chi^{(2)}_{spp}$ and $\chi^{(2)}_{psp}$ in these two formulae can be neglected and gives: $I_1 \approx C_1|\chi^{(2)}_{ssp}|^2$ and $I_2 \approx C_2|\chi^{(2)}_{ppp}|^2$. The SFG intensities of the DMPE monolayer at $\Omega = 45^\circ$ and $\Omega = -45^\circ$ were also collected by switching the polarization angle back and forth at each wavenumber. The calculated SFG intensity differences $R = \frac{\Delta I}{I} = \frac{I(\Omega = 45^\circ) - I(\Omega = -45^\circ)}{I(\Omega = 45^\circ) + I(\Omega = -45^\circ)}$ are very small, which indicate negligible contribution from $\chi^{(2)}_{psp}$ and $\chi^{(2)}_{spp}$ in SFG spectra collected at $\Omega = \pm 45^\circ$ and the validation of the simplified formulae given above.

**3.2.1 SFG spectra at different SPs.** Fig. 2 shows the SFG spectra of the DMPE and DPPE monolayers at surface pressures of 1 mN m$^{-1}$, 5 mN m$^{-1}$, 30 mN m$^{-1}$ and 50 mN m$^{-1}$ in the wavenumber range of 2800–3000 cm$^{-1}$. The vibrational peaks within this range mostly originate from $CH_2$ and $CH_3$ groups in the alkyl chains of the phospholipids. As seen in Fig. 2, the DMPE and DPPE monolayers show multiple characteristic peaks: $CH_2$-SS-*trans* ($\sim$2840 cm$^{-1}$, $\sim$2905 cm$^{-1}$), $CH_2$-SS-*gauche* ($\sim$2850 cm$^{-1}$, $\sim$2925 cm$^{-1}$), $CH_3$-SS ($\sim$2880 cm$^{-1}$), $CH_3$-Fermi ($\sim$2945 cm$^{-1}$), $CH_3$-AS ($\sim$2970 cm$^{-1}$).[22,23] It should also be noted that the small peak observed at $\sim$2905 cm$^{-1}$ ($\sim$2925 cm$^{-1}$ at lower SP) can be assigned to either CH group, or $CH_2$ groups in head groups (glycerol backbone, choline group). Such a small peak is also observed in the SFG spectra of an ODT monolayer (with no C–H group) at surface pressures of 5 mN m$^{-1}$ and 30 mN m$^{-1}$ (shown in Fig. S1, ESI†). Thus the peak at $\sim$2905 cm$^{-1}$ should be assigned to $CH_2$ groups.

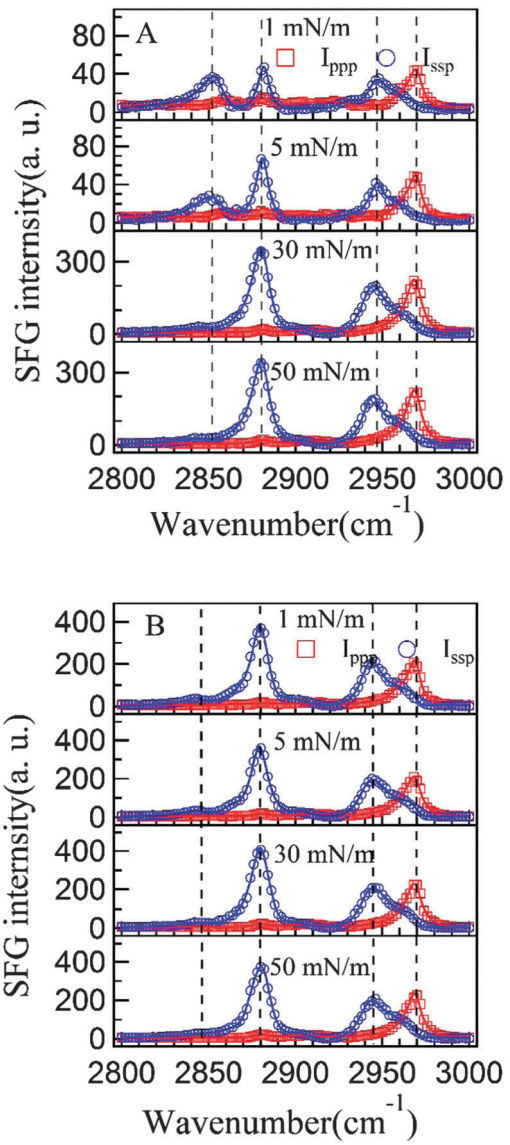


Fig. 2 SFG spectra of (A) DMPE monolayer and (B) DPPE monolayer at SP = 1 mN m$^{-1}$, 5 mN m$^{-1}$, 30 mN m$^{-1}$ and 50 mN m$^{-1}$ in the wavenumber range of 2800–3000 cm$^{-1}$.

By comparing the SFG spectra of the DMPE and DPPE monolayers at different SPs, it is easy to notice that all the spectra of the DPPE monolayers are very similar while the spectra of the DMPE monolayer at SP = 1 mN m$^{-1}$ and 5 mN m$^{-1}$ are different from the spectra at other SPs. All the SFG spectra of the DPPE monolayers show very small contributions of the $CH_2$-SS-*trans* peak at 2840 cm$^{-1}$, which indicates that the alkyl chains of DPPE molecules are well ordered from a very low SP. The similarity between SFG spectra also indicate that the conformation DPPE molecules are alike at different SPs, which is consistent with their lower compression elasticity compared to DMPE molecules. As with DMPE monolayers, the differences between the SFG spectra at various SP values indicate that DMPE molecules undergo much more conformational change during the compression. The spectra collected at SP = 1 mN m$^{-1}$ and 5 mN m$^{-1}$ (below the first plateau) show a significant contribution from the $CH_2$-SS peaks. The fitted widths of the $CH_2$-SS-*trans* in the tail groups and head groups are 36.0 $\pm$ 9.3 cm$^{-1}$ and 20.0 $\pm$ 6.8 cm$^{-1}$ respectively at SP = 1 mN m$^{-1}$. The peaks of $CH_2$-SS-*gauche* in tail groups and head groups are clearly seen in the spectra. Such spectroscopic characteristics indicate that the alkyl chains in the tail groups and head groups of DMPE molecules are randomly ordered or in a coiled conformation. Such a conformation also leads to much lower SFG intensities of the $CH_3$ group related peaks ($CH_3$-SS, $CH_3$-Fermi, $CH_3$-AS) compared to the intensities of the DPPE monolayer. Such a conformation should be the main reason that the DMPE BAM images show lower brightness in the LE phase. As the SP increases to 5 mN m$^{-1}$, the peak of $CH_2$-SS-*gauche* in the tail groups remains visible but the peak in the head groups are not seen from the spectra. The peak widths of $CH_2$-SS-*trans* in tail groups and head groups are 16.6 $\pm$ 4.1 cm$^{-1}$ and 9.5 $\pm$ 2.6 cm$^{-1}$ respectively.

The conformational changes of the DMPE molecules can also quantified by the fitting results of the SFG spectra of the DMPE monolayers at various SPs shown in Fig. 3. As seen in Fig. 3, the widths of the $CH_2$-*trans* peaks in the tail and head groups decrease as the MMA decreases, while the width of $CH_3$-SS peak increases as the MMA decreases upon compression. Such changes indicate that the conformation of the $CH_2$ groups becomes more rigid while the conformation of the $CH_3$ groups becomes less rigid during the compression. The peak amplitude of the $CH_3$-SS mode increases and the susceptibility

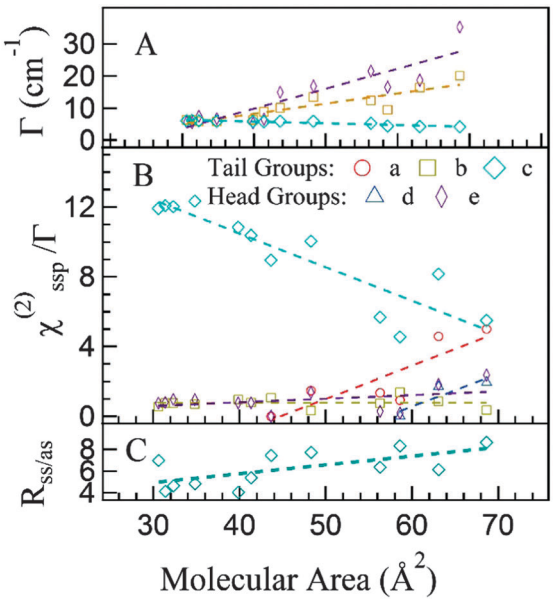


Fig. 3 The fitting results of SFG spectra of the DMPE monolayers at various SP. (A) Peak widths ($\Gamma$) of different vibration modes. (B) Peak amplitudes ($\chi^{(2)}_{ssp}/\Gamma$) of different vibration modes calculated from the fitting results, (C). Susceptibility ratio $\left(R_{SS/AS} = \chi^{(2)}_{ssp,CH_3\text{-}SS} \Big/ \chi^{(2)}_{ssp,CH_3\text{-}AS}\right)$ of methyl groups calculated from the fitting results. Tail groups: (a) $CH_2$-SS-*gauche*, (b) $CH_2$-SS-*trans*, (c) $CH_3$-SS, and head groups: (d) $CH_2$-SS-*gauche*, (e) $CH_2$-SS-*trans*.

ratio of $R_{ss/as} = \chi^{(2)}_{ssp,CH_3\text{-}SS} \Big/ \chi^{(2)}_{ssp,CH_3-AS}$ decreases as the MMA decreases. The peak width difference of the $CH_3$-SS mode between the LE phase ($4.9 \pm 0.2$ cm$^{-1}$) and the LC phase ($6.2 \pm 0.1$ cm$^{-1}$) also indicates that the tail group alkyl chain may adopt a coiled conformation rather than a randomly ordered conformation. If we assume that the all-*trans* conformations are rigidly formed in the LC phase, the chain tilt angle $\alpha$ with respect to the surface normal can be calculated by $\alpha = 41.5^\circ - \theta_{CH_3}$. The value of $\alpha$ is calculated to be $13.5 \pm 1.8^\circ$ at high SP.[22,24,49–51] The peak amplitudes of $CH_2$ groups (both $CH_2$-SS-*trans* and $CH_2$-SS-*gauche*) decrease as the MMA decreases. The disappearance of the tail group $CH_2$-SS-*gauche* mode and head group $CH_2$-SS-*gauche* mode at different MMA indicate that the conformational changes of the DMPE alkyl chains have separate stages: the reorientation of head group alkyl chains mostly happens in the LE phase, and the reorientation of tail group alkyl chains in mostly happens in the LE–LC phase.

**3.2.2 Conformational changes of DMPE molecules in the LE–LC phase.** The lipid conformations and molecular interactions in LE–LC phase are very important to membrane activities. The interaction between the LC and LE domains in the LE–LC phase were proven to be responsible for the double layer formation and squeezing out mechanism of the lung surfactant (DPPC).[52,53] The BAM images and SFG spectra of the DMPE monolayers at SP = 6, 7, 8, 9, 10 mN m$^{-1}$ (LE–LC phase) are shown in Fig. 4. As observed from Fig. 4, the bright domains in the DMPE BAM images become bigger as the SP

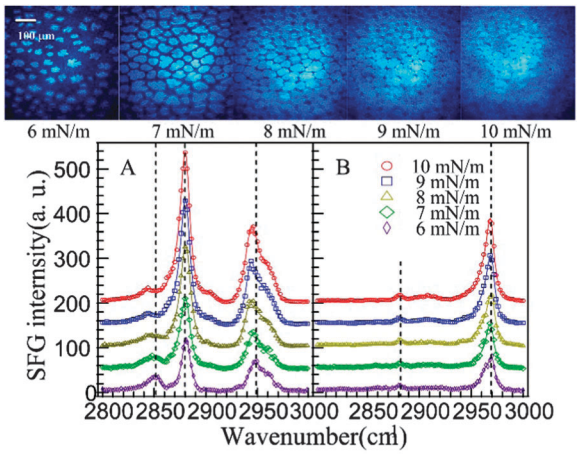


Fig. 4 BAM images and SFG spectra of DMPE monolayers at SP = 6, 7, 8, 9, 10 mN m$^{-1}$. (A) ssp spectra; (B) ppp spectra.

increases from 6 mN m$^{-1}$ to 10 mN m$^{-1}$, indicating an increasing phase transition percentage of the DMPE monolayer during compression. The amplitude of the $CH_3$-SS, $CH_3$-Fermi, $CH_3$-AS peaks increases gradually and the amplitude of the $CH_2$-SS-*trans* peak at 2840 cm$^{-1}$ becomes relatively smaller, which indicates that the ordering of alkyl chains has increased. The fitting results show that the amplitude of the $CH_2$-SS-*gauche* peak in tail groups reduces to zero at SP = 9 mN m$^{-1}$, indicating that the tail group alkyl chains of DMPE molecules are fully stretched (all-*trans*). The fully extended alkyl chains also result in a smaller inter-molecular distance and larger adhesive van der Waals force between DMPE molecules, as well as the formation of multiple lobed-shaped domains in the BAM images of the DMPE monolayer. Additionally, $\omega_{0,CH_3\text{-Fermi}}$ is downshifted by about $4.6 \pm 0.5$ cm$^{-1}$ as the SP of DMPE monolayer increases from 6 to 10 mN m$^{-1}$. As discussed in the literature, the $CH_3$-Fermi mode is generated by the energy level splitting of the $CH_3$-SS mode and the second overtone of the $CH_3$-bending mode, whose energy levels are very close to each other.[54,55] The decrease in the peak center wavenumber of the $CH_3$-Fermi mode indicates that the energy level of the $CH_3$-bending mode (second overtone) is lowered. The adhesive van der Waals force between the fully extended alkyl chains should be the main reason for the weakening of the vibrational force constant ($k$) of the $CH_3$-bending mode and the redshift of $\omega_{0,CH_3\text{-Fermi}}$. A similar redshift of $\omega_{0,Free\text{-}OH}$ ($\Delta\omega_0 = -20$ cm$^{-1}$) was also observed at water/OTS monolayer interface compared to the water/air interface.[56–58]

Additionally, the peak amplitude ratio between the $CH_3$-SS and $CH_3$-Fermi peaks $\left(R_{Fermi} = \dfrac{\chi^{(2)}_{CH_3\text{-SS}}/\Gamma_{CH_3\text{-SS}}}{\chi^{(2)}_{CH_3\text{-Fermi}}/\Gamma_{CH_3\text{-Fermi}}}\right)$ increases as the SP increases, but $\omega_{0,CH_3\text{-SS}}$ does not change significantly ($\Delta\omega_{0,CH_3\text{-SS}} = -0.4 \pm 0.2$ cm$^{-1}$) compared to the downshift of $\omega_{0,CH_3\text{-Fermi}}$. These experimental results indicate that either the contribution from Fermi resonance generated $CH_3$-SS peak is very small, or the influence of Fermi resonance effects on $\omega_{0,CH_3\text{-SS}}$ are compensated for by the effects of the adhesive van der Waals

 

forces. Further experiments are required to give a quantitative evaluation of the influence of the Fermi resonance effect on the frequency and amplitude of the $CH_3$-SS mode, as well as the van der Waals interactions between $CH_3$ groups.

### 3.3 Conformational changes of $PO_2^-$ groups

Fig. 5 shows SFG spectra of DMPE and DPPE monolayers at SP = 1 mN m$^{-1}$, 5 mN m$^{-1}$, 30 mN m$^{-1}$ and 50 mN m$^{-1}$ in the wavenumber range of 1000–1200 cm$^{-1}$. Two characteristic peaks are observed at ~1085 cm$^{-1}$ and ~1100 cm$^{-1}$, which originate from the R–O–P–O–R groups and $PO_2^-$ groups (symmetric stretching) respectively. However, the peak of C–OP at ~1050 cm$^{-1}$, which has been reported by Ma, G. *etc.* in previous literature, is too weak to be observed. It has also been reported that the peak positions of the $PO_2^-$-SS mode are very sensitive to the hydration state of lipid head groups.

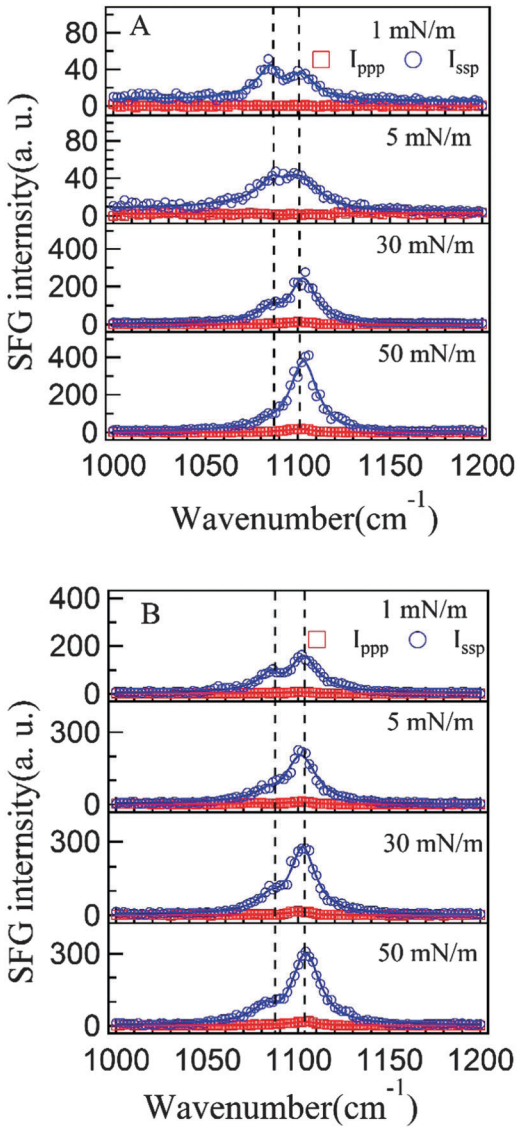


Fig. 5 SFG spectra of (A). DMPE monolayer and (B). DPPE monolayer at SP = 1 mN m$^{-1}$, 5 mN m$^{-1}$, 30 mN m$^{-1}$ and 50 mN m$^{-1}$ in the wavenumber range of 1000–1200 cm$^{-1}$.

The fitting results of SFG spectra indicate small blue-shifts of $PO_2^-$-SS peaks $\Delta\omega_{0,PO_2\text{-}SS}$ = 2.1 ± 0.5 cm$^{-1}$ when the SP increases, which indicates that the hydration states of $PO_2^-$ groups should be slightly changed. Similar phenomena were also observed by Ma, G. *etc.* using BB-SFG-VS in DPPC monolayers.[22,24]

The fitting results of SFG spectra also indicate that susceptibility ratios $R_{PO_2^-} = \chi^{(2)}_{ppp,PO_2^-\text{-}SS} \big/ \chi^{(2)}_{ssp,PO_2^-\text{-}SS}$ of DMPE and DPPE monolayers increase as the SP increases. The tilt angle dependence of $R_{PO_2^-}$ is plotted in Fig. S3 (ESI†). According to our data, the tilt angles of $PO_2^-$ groups in the DMPE molecule and DPPE molecule at SP = 1 mN m$^{-1}$ are close to 26°. And the tilt angles of $PO_2^-$ groups of DMPE and DPPE monolayers at SP = 50 mN m$^{-1}$ are 54.1 ± 6.8° and 46.8 ± 5.4° respectively.

### 3.4 Compression kinetics of the PE monolayer

The current polarization resolved SFG system is also capable of obtaining both molecular abundance and orientation based on the simultaneously collected ssp and ppp signals.[59–61] Such information can give a rough and quick estimation of molecular changes in the time domain, which would be very useful for understanding the kinetics of reaction, adsorption and desorption processes at the interface. Fig. 6 shows the compression kinetics of DMPE and DPPE monolayer monitored by the SP sensor and the polarization-resolved SFG system. The monitored wavenumbers were 2970 cm$^{-1}$ and 1105 cm$^{-1}$, which correspond to the characteristic vibrational peaks of the $CH_3$-AS and $PO_2^-$-SS modes respectively. As seen in Fig. 6, the increase of SP of DMPE and DPPE monolayers under a compression speed of 27 mm min$^{-1}$ follow a similar trend to the SP increase in the π–A isotherms (which were collected under compression speed of 5 mm min$^{-1}$). The plateau area of the DMPE monolayer at ~6 mN m$^{-1}$ is also shown in Fig. 4A. The change of $I^{2970cm^{-1}}$ from the DMPE monolayer can be separated into several stages: the first significant increase occurs at the end of the LE phase, followed by a gradual increase in the LE–LC phase, the second significant increase in the LC phase and the final plateau area at the end of the LC phase. It is interesting to note that the final plateau area of $I^{2970cm^{-1}}$ occurs at SP = 27 mN m$^{-1}$, which is much earlier than the final plateau of SP at ~55 mN m$^{-1}$. The fitted amplitudes of the $CH_3$-SS mode at various SP values in Fig. 3 show a similar trend. Such phenomena indicate that the conformation of the DMPE tail groups reaches equilibrium after SP reaches 27 mN m$^{-1}$ (at the beginning of the LC phase). BAM images of DMPE monolayers in the LC phase (shown in Fig. 1) indicate that the DMPE molecules are packed closely to form a monolayer with a uniform thickness. It is interesting that the surface pressure of most cell membranes is also maintained at ~30 mN m$^{-1}$. It has been reported that the phospholipid monolayer at such SPs can create an integral and elastic hydrophobic environment for protein insertion and functioning.[62] Cell membranes at such equilibrium states also provide a desirable barrier to separate the cellular activities from the influence of the extra-cellular environments. On the other hand, the change of $I^{1105cm^{-1}}$ from the DMPE monolayer is a little different: the first

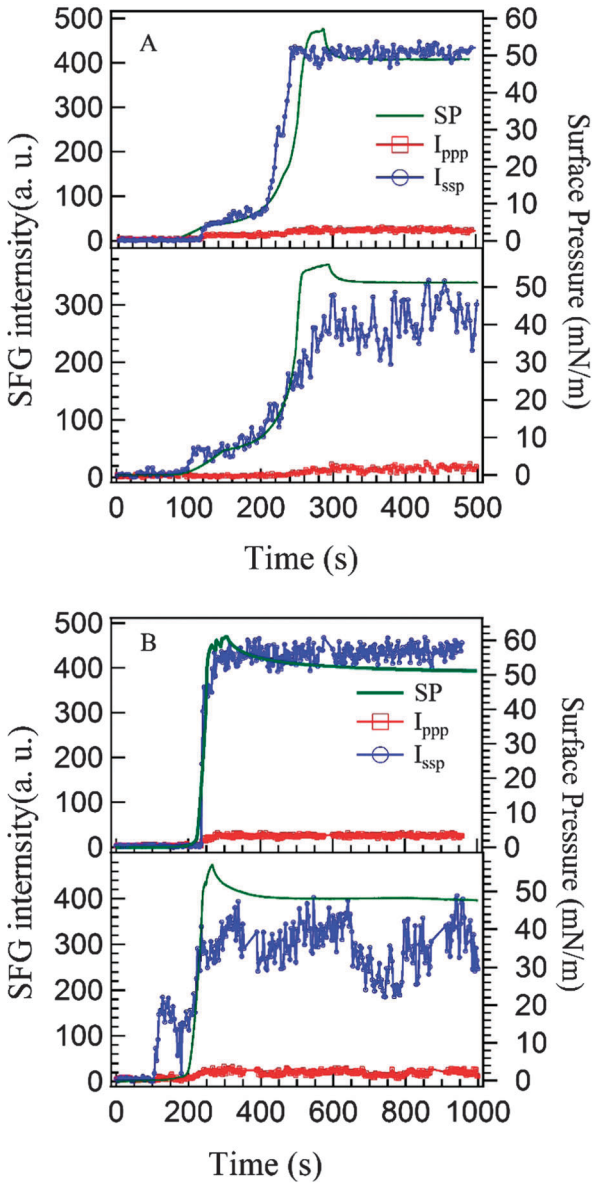


Fig. 6 Compression kinetics of (A) DMPE monolayer and (B) DPPE monolayer monitored by the SP sensor and polarization-resolved SFG system. Compression speed: 27 mm $min^{-1}$. Compressions stopped at ~60 mN $m^{-1}$. The SFG signals of both ssp and ppp polarization were collected at 2970 $cm^{-1}$ (upper) and 1105 $cm^{-1}$ (bottom) by averaging 50 pulses.

significant increase occurs at the beginning of the LE phase, and the final plateau area of $I^{1105cm^{-1}}$ occurs later than the final plateau area of the SP. It is understandable because the head groups of lipid molecules are usually placed at exterior areas of cell membranes, which are more susceptible to the environment. Similar trends are also seen in Fig. 6B, which presents the compression kinetics of the DPPE monolayer at 2970 $cm^{-1}$ and 1105 $cm^{-1}$.

The calculated SFG intensity ratios $R^{1105cm^{-1}} = I_{ssp}^{1105cm^{-1}} / I_{ppp}^{1105cm^{-1}}$ and $R^{2970cm^{-1}} = I_{ssp}^{2970cm^{-1}} / I_{ppp}^{2970cm^{-1}}$ are shown in Fig. S4 (ESI†). Despite the small contributions from non-resonant susceptibilities and other peaks $\left(I^{2970cm^{-1}} = C\left|\chi_{NR} + \chi_{CH_3\text{-Fermi}}^{2970cm^{-1}} + \chi_{CH_3\text{-AS}}^{2970cm^{-1}}\right|^2\right)$ and $\left(I^{1105cm^{-1}} = C\left|\chi_{NR} + \chi_{R-O-P-O-R}^{1105cm^{-1}} + \chi_{PO_2\text{-SS}}^{1105cm^{-1}}\right|^2\right)$, the SFG intensity ratios give a qualitative evaluation of the tilt angle changes of $CH_3$ groups. The rising points of $R^{1105cm^{-1}}$ and $R^{2970cm^{-1}}$ are clearly separated from the rising point from the SP curve. The difference between the compression kinetics of the PE monolayers detected at 2970 $cm^{-1}$ and 1105 $cm^{-1}$ indicate that the reorientation of $PO_2^-$ groups (head groups) and $-CH_3$ groups (tail groups) occur separately during the compression.

### 3.5 Relaxation kinetics of PE monolayers at high SP

Fig. 6 also shows the relaxation kinetics of PE monolayers after the compression stops at SP ≈ 60 mN $m^{-1}$. The decreasing curves of SP were fitted to a single exponential decay curve: $SP(t) = SP_0 + A\exp\left\{\frac{t - t_0}{\tau}\right\}$. The fitting gives $\tau$ = 7–10 s for the DMPE monolayer and $\tau$ = 50–60 s for the DPPE monolayer. Such difference in relaxation kinetics may either be due to different mobilities or different molecular interactions of DMPE and DPPE molecules at high SP. On the other hand, it is interesting to see that the values of $I_{CH_3\text{-AS}}^{2970cm^{-1}}$ remain stable despite the significant decrease of SP after stopping of the compression. Such information implies that the conformation of alkyl chains of PE molecules may remain stable during the monolayer relaxation, compatible with the experimental results mentioned above. This is possible because the molecular waist of the phospholipids is at the glycol groups, and not at the tail group alkyl chains. The molecular conformation of the phospholipids during the relaxation requires additional elucidations which will be addressed in our further publications.

## 4. Conclusions

In this study, the conformational changes and assembly behaviors of DMPE and DPPE molecules are investigated using a frequency-resolved and polarization-resolved picosecond SFG-VS system, combined with π–A isotherm and BAM detection. The compression kinetics and relaxation kinetics of PE monolayers are also measured. It is shown that the peak shift within few wavenumbers can be recognized using the current frequency-resolved SFG system. Based on the fitting parameters, the detailed conformational changes in methyl groups and dehydration of phosphate groups can be identified using such SFG systems. However, the signal to noise ratio is not good enough to distinguish the contributions of homogeneous and inhomogeneous lineshapes broadening from the fitting results.

It is revealed that the conformational changes of DMPE molecules during the monolayer compression could be separated into several stages: reorientation of the $PO_2^-$ group in head group at the beginning of the LE phase, conformational changes of head group alkyl chains (choline group) in the LE phase, conformational changes of tail group alkyl chains in the

 

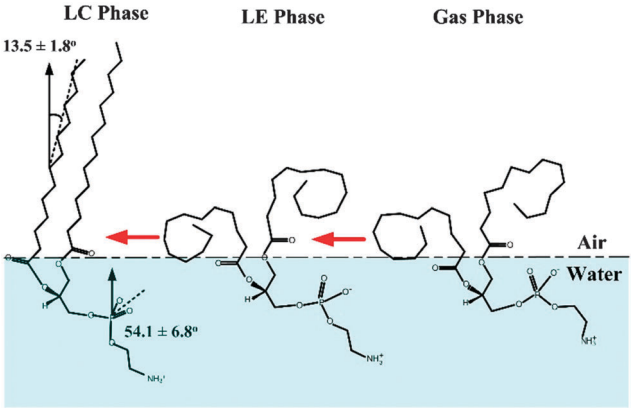


Scheme 3 Schematic illustration of the conformational changes of DMPE molecules at the air/water interface.

LE–LC phase. The conformational changes of DMPE molecules at the air/water interface are illustrated in Scheme 3. It has been reported that PE lipids tend to form non-lamellar membrane structures during the membrane fusion. After the reorientation of head group alkyl chains in the LE phase, the cone-shaped DMPE molecules may modulate the membrane curvature and facilitate the formation of non-lamellar phases of the cell membranes during the exocytosis/endocytosis processes. The current research study is the first step towards the understanding of the exocytosis behaviors and assembly behaviors of phosphatidylethanolamine (PE) molecules. The fine spectral resolution of our SFG system allowed us to distinguish the head groups and tail groups of PE molecules, and thus enabled us to understand its molecular behaviors during the formation of the exocytosis vesicles or the PE–DNA complexes. The understanding of compression kinetics and relaxation kinetics of PE lipids will also help researchers to effectively control the lipid molecular conformation and membrane curvatures.

## Acknowledgements

This work was supported by the Doctoral Program Foundation of Jianghan University (No. 1019-06100001). HCA acknowledges NSF-CHE (1111762) for partial funding of this work.

## Notes and references

1 J. E. Vance and G. Tasseva, *Biochim. Biophys. Acta*, 2013, **1831**, 543–554.
2 R. Steenbergen, *J. Biochem.*, 2005, **280**, 40032–40040.
3 A. Signorell, E. Gluenz, J. Rettig, A. Schneider, M. K. Shaw, K. Gull and P. Bütikofer, *Mol. Microbiol.*, 2009, **72**, 1068–1079.
4 Y. Uchiyama, M. M. Maxson, T. Sawada, A. Nakano and A. G. Ewing, *Brain Res.*, 2007, **1151**, 46–54.
5 H. Chakraborty, T. Sengupta and B. R. Lentz, *Biophys. J.*, 2014, **107**, 1327–1338.
6 E. I. Pécheur, I. Martin, O. Maier, U. Bakowsky, J. M. Ruysschaert and D. Hoekstra, *Biochemistry*, 2002, **41**, 9813–9823.
7 M. Schalke and M. Lösche, *Adv. Colloid Interface Sci.*, 2000, **88**, 243–274.
8 L. C. Gomes-da-Silva, N. A. Fonseca, V. Moura, M. C. Pedroso de Lima, S. Simoes and J. N. Moreira, *Acc. Chem. Res.*, 2012, **45**, 1163–1171.
9 S. Gromelski and G. Brezesinski, *Phys. Chem. Chem. Phys.*, 2004, **6**, 5551–5556.
10 M. A. Churchward, T. Rogasevskaia, D. M. Brandman, H. Khosravani, P. Nava, J. K. Atkinson and J. R. Coorssen, *Biophys. J.*, 2008, **94**, 3976–3986.
11 M. Langecker, V. Arnaut, J. List and F. C. Simmel, *Acc. Chem. Res.*, 2014, **47**, 1807–1815.
12 A. Zitzer, R. Bittman, C. A. Verbicky, R. K. Erukulla, S. Bhakdi, S. Weis, A. Valeva and M. Palmer, *J. Biol. Chem.*, 2001, **276**, 14628–14633.
13 C. A. Helm, P. Tippmann-Krayer, H. Möhwald, J. Als-Nielsen and K. Kjaer, *Biophys. J.*, 1991, **60**, 1457–1476.
14 X. Wang, H. Takahashi, I. Hatta and P. J. Quinn, *Biochim. Biophys. Acta*, 1999, **1418**, 335–343.
15 K. Czapla, B. Korchowiec and E. Rogalska, *Langmuir*, 2010, **26**, 3485–3492.
16 S. Gromelski and G. Brezesinski, *Langmuir*, 2006, **22**, 6293–6301.
17 X. D. Zhu, H. Suhr and Y. R. Shen, *Phys. Rev. B: Condens. Matter Mater. Phys.*, 1987, **35**, 3047–3050.
18 A. L. Harris, C. E. D. Chidsey, N. J. Levinos and D. N. Loiacono, *Chem. Phys. Lett.*, 1987, **141**, 350–356.
19 Y. R. Shen, *Nature*, 1989, **337**, 519–525.
20 S. Roke, J. Schins, M. Muller and M. Bonn, *Phys. Rev. Lett.*, 2003, **90**, 128101.
21 M. Bonn, S. Roke, O. Berg, L. B. F. Juurlink, A. Stamouli and M. Müller, *J. Phys. Chem. B*, 2004, **108**, 19083–19085.
22 G. Ma and H. C. Allen, *Langmuir*, 2006, **22**, 5341–5349.
23 G. Ma and H. C. Allen, *Langmuir*, 2006, **22**, 11267–11274.
24 G. Ma and H. C. Allen, *Langmuir*, 2007, **23**, 589–597.
25 N. N. Casillas-Ituarte, X. Chen, H. Castada and H. C. Allen, *J. Phys. Chem. B*, 2010, **114**, 9485–9495.
26 M. Sovago, G. W. Wurpel, M. Smits, M. Muller and M. Bonn, *J. Am. Chem. Soc.*, 2007, **129**, 11079–11084.
27 P. Viswanath, A. Aroti, H. Motschmann and E. Leontidis, *J. Phys. Chem. B*, 2009, **113**, 14816–14823.
28 G. W. Wurpel, M. Sovago and M. Bonn, *J. Am. Chem. Soc.*, 2007, **129**, 8420–8421.
29 I. I. Rzeznicka, M. Sovago, E. H. G. Backus, M. Bonn, T. Yamada, T. Kobayashi and M. Kawai, *Langmuir*, 2010, **26**, 16055–16062.
30 C. Ohe, Y. Goto, M. Noi, M. Arai, H. Kamijo and K. Itoh, *J. Phys. Chem. B*, 2007, **111**, 1693–1700.
31 P. J. Kett, M. T. Casford and P. B. Davies, *Langmuir*, 2010, **26**, 9710–9719.
32 P. J. Kett, M. T. Casford and P. B. Davies, *J. Phys. Chem. B*, 2011, **115**, 6465–6473.
33 P. J. Kett, M. T. Casford and P. B. Davies, *J. Chem. Phys.*, 2013, **138**, 225101.

34 P. J. Kett, M. T. Casford and P. B. Davies, *J. Phys. Chem. B*, 2013, **117**, 6455–6465.
35 I. V. Stiopkin, H. D. Jayathilake, A. N. Bordenyuk and A. V. Benderskii, *J. Am. Chem. Soc.*, 2008, **130**, 2271–2275.
36 M. Sovago, E. Vartiainen and M. Bonn, *J. Chem. Phys.*, 2009, **131**, 161107.
37 X. Chen, W. Hua, Z. Huang and H. C. Allen, *J. Am. Chem. Soc.*, 2010, **132**, 11336–11342.
38 J. A. Mondal, S. Nihonyanagi, S. Yamaguchi and T. Tahara, *J. Am. Chem. Soc.*, 2010, **132**, 10656–10657.
39 M. Smits, M. Sovago, G. W. H. Wurpel, D. Kim, M. Muller and M. Bonn, *J. Phys. Chem. C*, 2007, **111**, 8878–8883.
40 S. Yamamoto, A. Ghosh, H. K. Nienhuys and M. Bonn, *Phys. Chem. Chem. Phys.*, 2010, **12**, 12909–12918.
41 L. Fu, Y. Zhang, Z. H. Wei and H. F. Wang, *Chirality*, 2014, **26**, 509–520.
42 L. Velarde and H. F. Wang, *J. Chem. Phys.*, 2013, **139**, 084204.
43 L. Velarde and H. F. Wang, *Phys. Chem. Chem. Phys.*, 2013, **15**, 19970–19984.
44 L. Velarde and H. F. Wang, *Chem. Phys. Lett.*, 2013, **585**, 42–48.
45 B. C. Johnson, V. J. Newell, J. B. Clark and E. S. McPhee, *J. Opt. Soc. Am. B*, 1995, **12**, 2122–2127.
46 K. Hoda, Y. Ikeda, H. Kawasaki, K. Yamada, R. Higuchi and O. Shibata, *Colloids Surf., B*, 2006, **52**, 57–75.
47 M. Minones, O. Conde, J. M. Trillo and J. Minones, *J. Phys. Chem. B*, 2010, **114**, 10774–10781.
48 F. Wei, Y. Y. Xu, Y. Guo, S. L. Liu and H. F. Wang, *Chin. J. Chem. Phys.*, 2009, **22**, 592–600.
49 W. Gan, B. H. Wu, Z. Zhang, Y. Guo and H. F. Wang, *J. Phys. Chem. C*, 2007, **111**, 8716–8725.
50 W. Gan, Z. Zhang, R. R. Feng and H. F. Wang, *J. Phys. Chem. C*, 2007, **111**, 8726–8738.
51 H. F. Wang, W. Gan, R. Lu, Y. Rao and B. H. Wu, *Int. Rev. Phys. Chem.*, 2005, **24**, 191–256.
52 I. C. Shieh and J. A. Zasadzinski, *Proc. Natl. Acad. Sci. U. S. A.*, 2015, **112**, E826–E835.
53 P. Dhar, E. Eck, J. N. Israelachvili, D. W. Lee, Y. Min, A. Ramachandran, A. J. Waring and J. A. Zasadzinski, *Biophys. J.*, 2012, **102**, 56–65.
54 T. W. Zerda, M. Bradley and J. Jonas, *Chem. Phys. Lett.*, 1985, **117**, 566–570.
55 J. C. Lavalley and N. Sheppard, *Spectrochim. Acta, Part A*, 1972, **28**, 2091–2101.
56 C. S. Tian and Y. R. Shen, *Proc. Natl. Acad. Sci. U. S. A.*, 2009, **106**, 15148–15153.
57 L. F. Scatena, M. G. Brown and G. L. Richmond, *Science*, 2001, **292**, 908–912.
58 F. W. Delrio, M. P. de Boer, J. A. Knapp, E. David Reedy, Jr., P. J. Clews and M. L. Dunn, *Nat. Mater.*, 2005, **4**, 629–634.
59 X. Chen, J. Wang, C. B. Kristalyn and Z. Chen, *Biophys. J.*, 2007, **93**, 866–875.
60 F. Wei and S. J. Ye, *J. Phys. Chem. C*, 2012, **116**, 16553–16560.
61 F. Wei, S. Ye, H. Li and Y. Luo, *J. Phys. Chem. C*, 2013, **117**, 11095–11103.
62 D. Marsh, *Biophys. J.*, 2007, **93**, 3884–3899.

 